

**PUBLISHED VERSION**

Self-consistent nonlinear kinetic simulations of the anomalous Doppler instability of suprathermal electrons in plasmas

W. N. Lai, S. C. Chapman, and R. O. Dendy

© 2013 UNITED KINGDOM ATOMIC ENERGY AUTHORITY.

This article may be downloaded for personal use only. Any other use requires prior permission of the author and the American Institute of Physics. The following article appeared in *Physics of Plasmas* **20**, 102122 (2013); and may be found at <http://dx.doi.org/10.1063/1.4827207>



**Self-consistent nonlinear kinetic simulations of the anomalous Doppler instability of suprathermal electrons in plasmas**

W. N. Lai, S. C. Chapman, and R. O. Dendy

Citation: [Physics of Plasmas \(1994-present\)](#) **20**, 102122 (2013); doi: 10.1063/1.4827207

View online: <http://dx.doi.org/10.1063/1.4827207>

View Table of Contents: <http://scitation.aip.org/content/aip/journal/pop/20/10?ver=pdfcov>

Published by the [AIP Publishing](#)

---



## Re-register for Table of Content Alerts

Create a profile.



Sign up today!



# Self-consistent nonlinear kinetic simulations of the anomalous Doppler instability of suprathermal electrons in plasmas

W. N. Lai,<sup>1</sup> S. C. Chapman,<sup>1,2</sup> and R. O. Dendy<sup>1,3</sup>

<sup>1</sup>Centre for Fusion, Space and Astrophysics, Department of Physics, University of Warwick, Coventry CV4 7AL, United Kingdom

<sup>2</sup>Department of Mathematics and Statistics, University of Tromsø, Tromsø, Norway

<sup>3</sup>Euratom/CCFE Fusion Association, Culham Science Centre, Abingdon, Oxfordshire OX14 3DB, United Kingdom

(Received 6 September 2013; accepted 14 October 2013; published online 30 October 2013)

Suprathermal tails in the distributions of electron velocities parallel to the magnetic field are found in many areas of plasma physics, from magnetic confinement fusion to solar system plasmas. Parallel electron kinetic energy can be transferred into plasma waves and perpendicular gyration energy of particles through the anomalous Doppler instability (ADI), provided that energetic electrons with parallel velocities  $v_{\parallel} \geq (\omega + \Omega_{ce})/k_{\parallel}$  are present; here  $\Omega_{ce}$  denotes electron cyclotron frequency,  $\omega$  the wave angular frequency, and  $k_{\parallel}$  the component of wavenumber parallel to the magnetic field. This phenomenon is widely observed in tokamak plasmas. Here, we present the first fully self-consistent relativistic particle-in-cell simulations of the ADI, spanning the linear and nonlinear regimes of the ADI. We test the robustness of the analytical theory in the linear regime and follow the ADI through to the steady state. By directly evaluating the parallel and perpendicular dynamical contributions to  $\mathbf{j} \cdot \mathbf{E}$  in the simulations, we follow the energy transfer between the excited waves and the bulk and tail electron populations for the first time. We find that the ratio  $\Omega_{ce}/(\omega_{pe} + \Omega_{ce})$  of energy transfer between parallel and perpendicular, obtained from linear analysis, does not apply when damping is fully included, when we find it to be  $\omega_{pe}/(\omega_{pe} + \Omega_{ce})$ ; here  $\omega_{pe}$  denotes the electron plasma frequency. We also find that the ADI can arise beyond the previously expected range of plasma parameters, in particular when  $\Omega_{ce} > \omega_{pe}$ . The simulations also exhibit a spectral feature which may correspond to the observations of suprathermal narrowband emission at  $\omega_{pe}$  detected from low density tokamak plasmas. © 2013 AIP Publishing LLC. [<http://dx.doi.org/10.1063/1.4827207>]

## I. INTRODUCTION

The anomalous Doppler instability (ADI)<sup>1–15</sup> is a key limiting mechanism for suprathermal tails in the probability distribution of the component of electron velocity parallel to the magnetic field direction,  $v_{\parallel}$ , in a plasma. It has been found in over four decades of experiments in low density tokamak plasmas<sup>4–8,11,14</sup> with both Ohmic and lower hybrid current drive, and remains topical. For example, the ADI is believed to explain the recently observed relaxation oscillations in directional hard X-ray signals emitted by the energetic electron population in the HT-7 tokamak.<sup>14,15</sup> These observations reflect the underlying physics of the ADI, which involves a shift of energy from parallel to perpendicular particle motion, accompanied by the excitation of waves at frequency and wavenumber  $(\omega, \mathbf{k})$  satisfying the anomalous Doppler resonance condition<sup>11</sup>

$$\omega - \mathbf{k} \cdot \mathbf{v} = n\Omega, \quad (1)$$

where  $\Omega$  is the cyclotron frequency and  $\mathbf{v}$  is particle velocity, specifically  $n = -1$  is the ADI. Analytical theory of the linear ADI confirms that in plasmas, this applies at both the classical single-particle level<sup>12</sup> and the collective level<sup>9,10</sup> of mathematical description. Oscillations in the amplitude of the directional X-ray signal observed from tokamaks, reported most recently in Ref. 14, are believed to arise where the

energetic electron tail distribution undergoes repeated cycles of relaxations through the isotropising effect of the ADI in its fully nonlinear regime, followed by re-extension of the tail by the current drive processes. Importantly, the ADI can occur for tail distributions that are monotonically decreasing in the  $v_{\parallel}$  direction. In this respect, the ADI differs fundamentally from inverse Landau damping as a limiting mechanism for tail distributions. Here, we present, for the first time, a fully nonlinear kinetic treatment of the ADI for the electron population with parameters and topologies relevant to magnetically confinement fusion. By means of a well diagnosed large-scale particle-in-cell (PIC) code,<sup>16</sup> we explore how the full combined bulk and tail electron velocity distribution, together with the self-consistently excited electromagnetic fields, evolve in time and depend on plasma parameters. This is an essential step towards exploiting the potential of the anomalous Doppler effect as a spontaneous *in situ* diagnostic of tokamak plasma electron populations. It may also contribute to the diagnostic and design capability for planned beam-plasma experiments in this area.<sup>17,18</sup> The anomalous Doppler instability is of interest in space plasmas, see for example Ref. 19, and is closely related<sup>20</sup> to the instability occurring at the inner Lindblad resonance in spiral galaxies.

In this paper, we study the evolution of the combined bulk and energetic electron distribution, and of the characteristics of the excited waves, throughout the ADI. We focus

primarily on flat tail electron distributions, and compare analytical linear growth rates with simulation results at early and later times, for different percentages  $\xi$  of energetic electrons and for different magnetic field orientations. We then track the energy transfer between excited waves and the tail and bulk electron populations by evaluation of  $\mathbf{j} \cdot \mathbf{E}$  through and beyond the linear regime.

## II. THE LINEAR ANOMALOUS DOPPLER INSTABILITY

We will first use linear theory to establish the regime in which the ADI will operate in our simulations. The theory of the ADI can be considered at different levels of description, quantum,<sup>1,3</sup> classical single particle,<sup>12</sup> and collective.<sup>2,4–10</sup> The conservation of energy between the longitudinal kinetic energy and the oscillator energy in quantum wave emission by electrons in a magnetic field in the nonrelativistic limit is given by

$$\Delta\epsilon = \hbar\omega_k = \Delta p_{\parallel}v_{\parallel} + n\hbar\Omega_{ce}, \quad (2)$$

where  $\Omega_{ce} = |q_e|B/m_e$  is the electron cyclotron frequency,  $q_e$  and  $m_e$  are the electron charge and mass, respectively; and  $\hbar$  is the reduced Planck's constant. This can be expressed as

$$\omega_k - k_{\parallel}v_{\parallel} = n\Omega_{ce}. \quad (3)$$

The preceding equation defines the condition for cyclotron resonances, where  $n=0$  corresponds to the Cerenkov-Landau resonance, and positive and negative  $n$  refer to normal and anomalous Doppler cyclotron resonances respectively. When  $n=-1$ , the resonant parallel velocity  $v_{\parallel} = v_{AD} = (\omega_k + \Omega_{ce})/k_{\parallel}$ . If the suprathermal electron population is such that there is a finite number of electrons having  $v_{\parallel} \geq v_{AD}$ , the ADI will occur provided that other counteracting effects, notably Landau damping, are overcome.

At the single particle level of description using linear analysis, the energy flows associated with an electron undergoing anomalous Doppler instability in a magnetised plasma are as follows: from the kinetic energy of motion parallel to the magnetic field direction, into the kinetic energy of motion perpendicular to the external magnetic field  $\mathbf{B}$  and into wave energy of the resonant excited electrostatic wave, in the ratio  $\Omega_{ce} : \omega_{pe}$ . The driving contribution to the total linear growth rate scales with the magnitude of the tail

distribution, integrated over perpendicular velocity, at the anomalous Doppler resonant parallel velocity. For net linear growth to exist, the corresponding Landau resonant velocity of the excited wave must lie beyond the bulk thermal population, otherwise linear Landau damping is usually sufficient to overcome the drive, thereby preventing the instability. These features carry over into the linear analysis of collective energy flows calculated from  $\mathbf{j} \cdot \mathbf{E}$ . The rates at which work is done by the electrostatic field on the components of electron motion parallel and perpendicular to the magnetic field,  $R_{\parallel}$  and  $R_{\perp}$ , are given by the following expressions in the linear regime:<sup>10</sup>

$$R_{\perp} = \mathbf{j}_{\perp} \cdot \mathbf{E}_{\perp} = \left(\frac{|E|}{4\pi}\right) 2\gamma_{AD} \frac{\Omega_{ce}}{\omega_{pe}}, \quad (4)$$

$$R_{\parallel} = \mathbf{j}_{\parallel} \cdot \mathbf{E}_{\parallel} = \frac{|E|^2}{4\pi} \left(2\gamma_{LB} + 2\gamma_{LT} - 2\left(1 + \frac{\Omega_{ce}}{\omega_{pe}}\right)\gamma_{AD}\right). \quad (5)$$

In the case when the anomalous growth rate,  $\gamma_{AD}$ , is greater than the Landau damping by the tail and bulk populations,  $\gamma_{LT}$  and  $\gamma_{LB}$ , it follows that  $R_{\parallel}$  is negative while  $R_{\perp}$  is positive. This implies that parallel electron kinetic energy is transferred to waves propagating in the parallel direction, which also mediate the transfer of electron parallel kinetic energy into the perpendicular direction.

For the ADI to occur, it is essential that electron and ion Landau damping of the resonant wave is weaker than the driving term. Figure 1 shows the analytical linear growth rate of electrostatic waves derived from Eq. (A3) to (A7) for an electron distribution with a flat suprathermal tail, represented analytically by Eq. (A2) combined with

$$F(v_{\parallel}) = \frac{1}{v_M}, \quad 0 \leq v_{\parallel} \leq v_M, \quad (6)$$

with  $v_M \approx 17v_B$ ,  $v_{T\perp} = v_B$ , and  $\Omega_{ce}/\omega_{pe} = 1.31$ . There is a well-defined region in  $(k_{\perp}, k_{\parallel})$  space where the ADI occurs. The boundary at small  $k_{\parallel}$  in Fig. 1 reflects the maximum velocity at which electrons are present in the tail, whereas growth at large  $k$  is prevented by Landau damping.

In the case of a cold magnetised plasma, there are two normal modes of electrostatic oscillations, with characteristic upper and lower frequencies  $\omega_1$  and  $\omega_2$  given by<sup>21</sup>

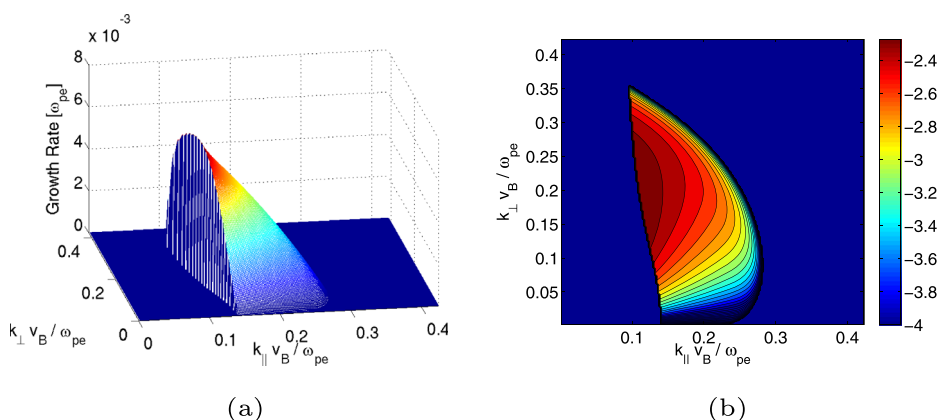


FIG. 1. Analytical linear growth rate of the ADI calculated from Eqs. (A3)–(A7) for an electron distribution with a 10% flat tail, shown in: (a) 3D plot; (b) contour plot, in  $(k_{\parallel}, k_{\perp})$  space. The growth rates are shown in units of  $\omega_{pe}$ . See main text for model parameters.

$$\omega_{1,2}^2 = \frac{\omega_{UH}^2}{2} \pm \frac{1}{2}(\omega_{UH}^4 - 4\Omega_{ce}^2\omega_{pe}^2 \cos^2 \theta)^{1/2}. \quad (7)$$

Here  $\omega_1$  relates to the + root and  $\omega_{UH} = (\Omega_{ce} + \omega_{pe})^{1/2}$  is the upper hybrid frequency,  $\theta$  denotes the angle between the magnetic field  $\mathbf{B}$  and the wavevector  $\mathbf{k}$ .

### III. SIMULATION METHOD

Computational study of the nonlinear evolution of an electron population undergoing anomalous Doppler instability, and of the character of the excited fields, is carried out here using PIC simulations with one spatial and three velocity coordinates (1D3V). We use the EPOCH PIC code,<sup>16</sup> where full ion and electron dynamics of macroparticles with velocity  $\mathbf{v}(x, t)$ , together with  $\mathbf{E}(x, \mathbf{v}, t)$  and  $\mathbf{B}(x, \mathbf{v}, t)$ , evolve self-consistently under the Lorentz force law and relativistic Maxwell equations on staggered grids with periodic boundary conditions. All electron characteristic lengthscales, including Debye length and gyro-radius, are resolved in the simulations. The suprathermal electron parallel velocity distribution in Eq. (A2) is initially modelled to be either flat as in Eq. (6), or monotonically decreasing, using superposition of drifted Maxwellians:

$$F(v_{\parallel}) = \frac{1}{\pi^{1/2}v_T} e^{-(v_{\parallel}-v_D)^2/v_T^2}, \quad (8)$$

where  $v_D$  is the drift velocity of the energetic electron population, and  $v_T$  is its thermal spread.

In these simulations, we initialise with a suprathermal electron tail extending to velocities up to  $15v_B - 30v_B$ , where  $v_B$  represents the thermal velocity of the Maxwellian bulk electrons. The tail contains a small fraction  $\xi$  of the total electron population, in the range of 1%–10%. We adopt the method of particle splitting, such that same number of macroparticles are used in both the bulk and the tail populations to ensure sufficient statistical sampling of the tail distribution. The direction of the background magnetic field, and hence of the electron tail distribution, is oriented at an angle,  $\theta = 45^\circ$  in our simulations, to the 1D spatial simulation domain. This allows both  $k_{\parallel}$  and  $k_{\perp}$  components relative to the magnetic field to be captured in the simulation; finite  $k_{\perp}$  is an essential condition for the ADI. The parameters including temperature, density, and magnetic field strength are chosen such that the ADI conditions are satisfied. The highly asymmetric electron tail population has non-zero mean parallel velocity, so the thermal bulk is slightly shifted such that the rest frame of the simulations has no net velocity with respect to the mean velocity of the combined electron distribution.

One of the main difficulties in reproducing the ADI using self-consistent simulations with  $\xi \ll 1$  is that the initial growth rates are relatively small compared to the characteristic oscillation frequency, usually of the order of  $\gamma = 10^{-2.5}\omega_{pe} - 10^{-4}\omega_{pe}$ . Thus, computationally expensive long timescale simulations are required. In the present simulations, the ratio  $\Omega_{ce}/\omega_{pe}$  ranges between 0.5 and 2.0. This range of  $\Omega_{ce}/\omega_{pe}$  is chosen to achieve balance between speed and resolution of the simulations. We note that  $\Omega_{ce}/\omega_{pe}$  is

equivalent to  $\lambda_D/\lambda_L$  which determines the grid sizes of the simulations, where  $\lambda_D$  is the electron Debye length and  $\lambda_L$  represents the electron Larmor radius.

The physical parameters used in the simulations, unless otherwise specified, are  $|\mathbf{B}| = 1.35 \times 10^{-7}\text{T}$ ,  $n_e = 1.0 \times 10^5 \text{ m}^{-3}$ ,  $T_B = 3.0 \times 10^5 \text{ K}$ ,  $\omega_{pe} = 1.8 \times 10^4 \text{ rads}^{-1}$ , and  $\Omega_{ce} = 2.36 \times 10^4 \text{ rads}^{-1}$ . Typically the spatial simulation domain encompasses 50 000 cells containing  $10 \times 10^6$  macroparticles. While our main aim in this paper is to understand the physics of the ADI, the simulation parameters can be extended to tokamak-like or other plasma conditions, albeit at some computational cost. The physical parameters correspond to  $\Omega_{ce} \sim \omega_{pe}$ , which is also the case in typical realisations of ADI in tokamak experiments. However, analytical estimates of the growth rates (see Appendix and Ref. 10) are in the limit  $\Omega_{ce} \gg \omega_{pe}$ . Whilst this limit does not strictly hold in our simulations, the analysis nonetheless provides an order of magnitude benchmark.

### IV. TIME EVOLUTION OF PARTICLES AND FIELDS UNDER THE ANOMALOUS DOPPLER INSTABILITY

Figure 2 shows the time sequence of plots of an electron distribution function evolving from pencil-like to pancake-like under the action of the ADI. The constant- $f$  contours for the highest energy component of the electron population, initially extended in the direction of the parallel velocity axis, spread rapidly in the perpendicular velocity direction. Owing to wave excitation, not all the parallel kinetic energy dissipated can be transferred to the perpendicular component. Hence the spreading of  $f$  in  $(v_{\parallel}, v_{\perp})$  does not follow the kinetic energy conserving path, that is indicated by contours shown in dashed lines in Fig. 2. Initially, the electron tail population at higher  $v_{\parallel}$  spreads out into  $v_{\perp}$  at a higher rate than the tail population at lower  $v_{\parallel}$ , which remains almost unchanged and can be seen from panels (a)–(e) in Fig. 2. Modes for which  $v_{AD}$  lies at smaller  $v_{\parallel}$  do not arise at early linear stages, due to Landau damping by the thermal bulk. Figure 2 also shows local flattening and parallel extension of the bulk distribution at a few  $v_B$ , which is a consequence of Landau damping there of tail-excited waves. We note that this effect can only be captured quantitatively by self-consistent nonlinear simulations, and is beyond the reach of linear or quasilinear analysis.

To characterise the excited waves and how they develop throughout the ADI, the corresponding structure of the electrostatic field amplitude in  $(\omega, k)$  space is shown in the sequence of plots in Fig. 3, where each panel corresponds to the time interval between two snapshots in Fig. 2. Figure 3 enables the identification of the excited modes from their dispersion relations. It also shows how the frequencies of the most strongly driven modes change in time, as the ADI proceeds through its linear phase into its nonlinear phase. Panels (a)–(g) of Fig. 3 correspond to the linear phase of ADI, during which the intensity of the two forward propagating electrostatic modes, marked as A and B in panels (b)–(d), increases exponentially. The two backward propagating modes are Langmuir waves in uniform magnetised plasma,  $\omega_1$  and  $\omega_2$  from Eq. (7). The characteristic frequencies of the

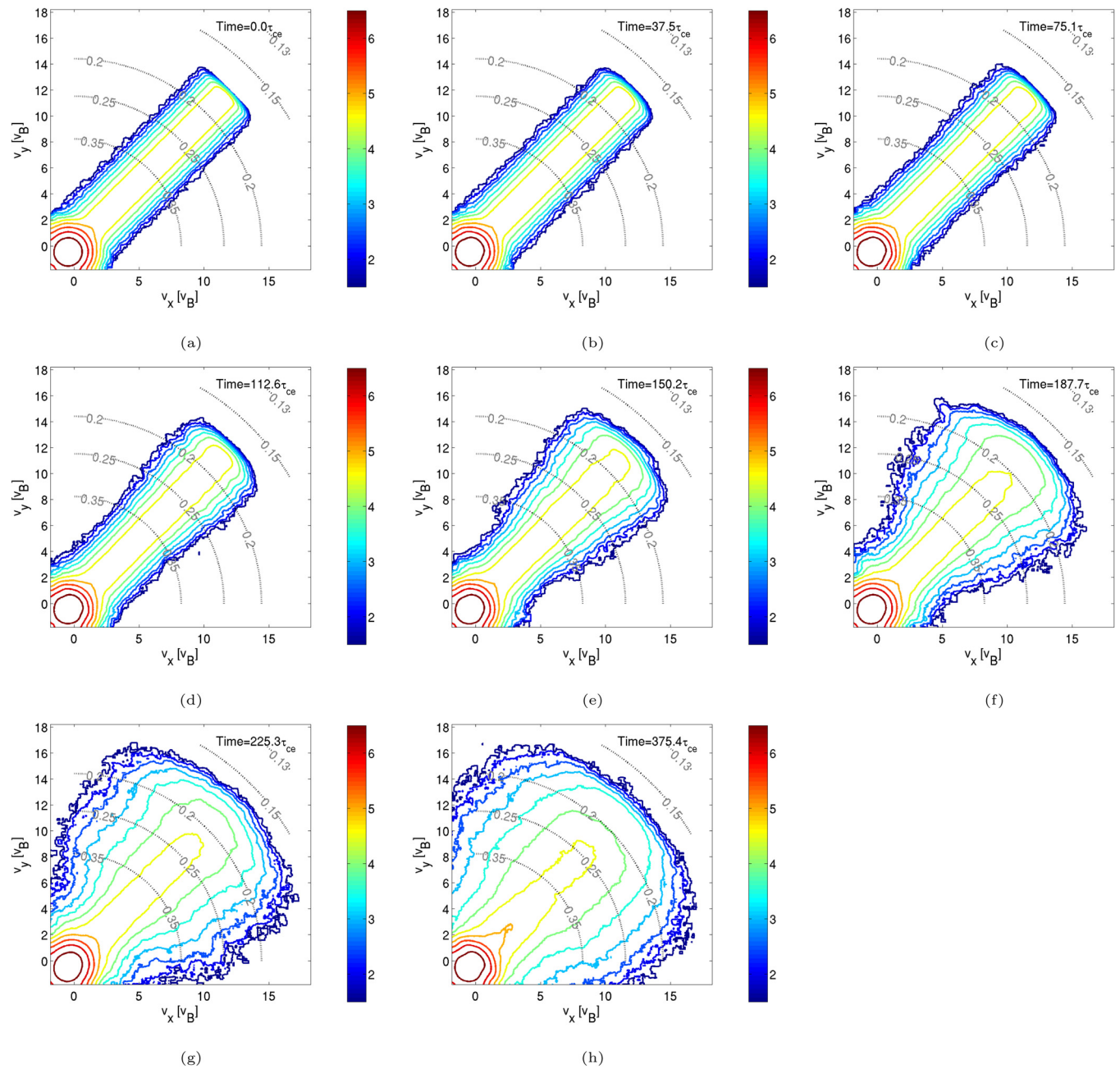


FIG. 2. Self-consistent spreading of the high energy tail of an electron distribution undergoing ADI, orientated at  $45^\circ$  to the magnetic field direction. Constant- $f$  contour plots of the time evolution of an electron distribution with  $\xi = 0.08$  of the population in an initially flat tail in  $(v_x, v_y)$  phase space; velocities are in units of thermal velocity. Here  $\Omega_{ce}/\omega_{pe} = 1.31$ , and the tail model in Eq. (6) is used, with  $v_M/v_B = 17$ . The colour density is in logarithmic scale with overlaying dash lines that represent the constant  $v$  surfaces with normalised wavenumber  $kv_B/\omega_{pe}$  inferred from Eq. (3). Panels (a) to (h) show snapshots from initial setup, through linear instability, to the nonlinear phase of the ADI:  $t =$  (a)  $0.0 \tau_{ce}$ , (b)  $37.5 \tau_{ce}$ , (c)  $75.1 \tau_{ce}$ , (d)  $112.6 \tau_{ce}$ , (e)  $150.2 \tau_{ce}$ , (f)  $187.7 \tau_{ce}$ , (g)  $225.3 \tau_{ce}$  and (h)  $375.4 \tau_{ce}$ , where  $\tau_{ce}$  is the electron cyclotron period,  $\tau_{ce} = 2\pi/\Omega_{ce}$ . Panels (a) to (g) are separated by equal time intervals,  $37.5 \tau_{ce}$ , where the last two panels are separated by a longer time interval,  $150.1 \tau_{ce}$ . This is to reflect the relatively slow evolution of the electron distribution in the later stage of the simulation. Different phases of the ADI are identified from the electric field amplitude in Fig. 7, where the linear and nonlinear phases correspond to the exponential growth and saturation phases of the electric field amplitude, respectively. The electron distributions are first binned at a resolution of  $\Delta v \approx 0.04 v_B$  and then smoothed using averaging over four nearest neighbours.

two forward propagating modes, A and B in Fig. 3, roughly correspond to these Langmuir modes,  $\omega_1$  and  $\omega_2$ , but slightly adjusted by relatively large asymmetric electron tail,  $\xi = 0.08$  in this case. An electrostatic mode appears at approximately  $\omega \approx \omega_{pe}$  in the later stages of the linear phase, marked as C in panels (d)–(g), but vanishes in the nonlinear phase as shown in panel (h). The physical origin of the feature at  $\omega \approx \omega_{pe}$  in panels (d) to (g) of Fig. 3 is uncertain. It

appears that inverse Landau damping and BGK modes can be excluded, because the velocity distribution is always monotonically decreasing with respect to  $v_{\parallel}$  and there is no evidence for particle trapping. This spectral feature of our simulations may correspond to the observations of fluctuating narrowband emission at  $\omega_{pe}$  from low density tokamak plasmas with extended suprathermal electron tails; see, for example, Refs. 22–26.

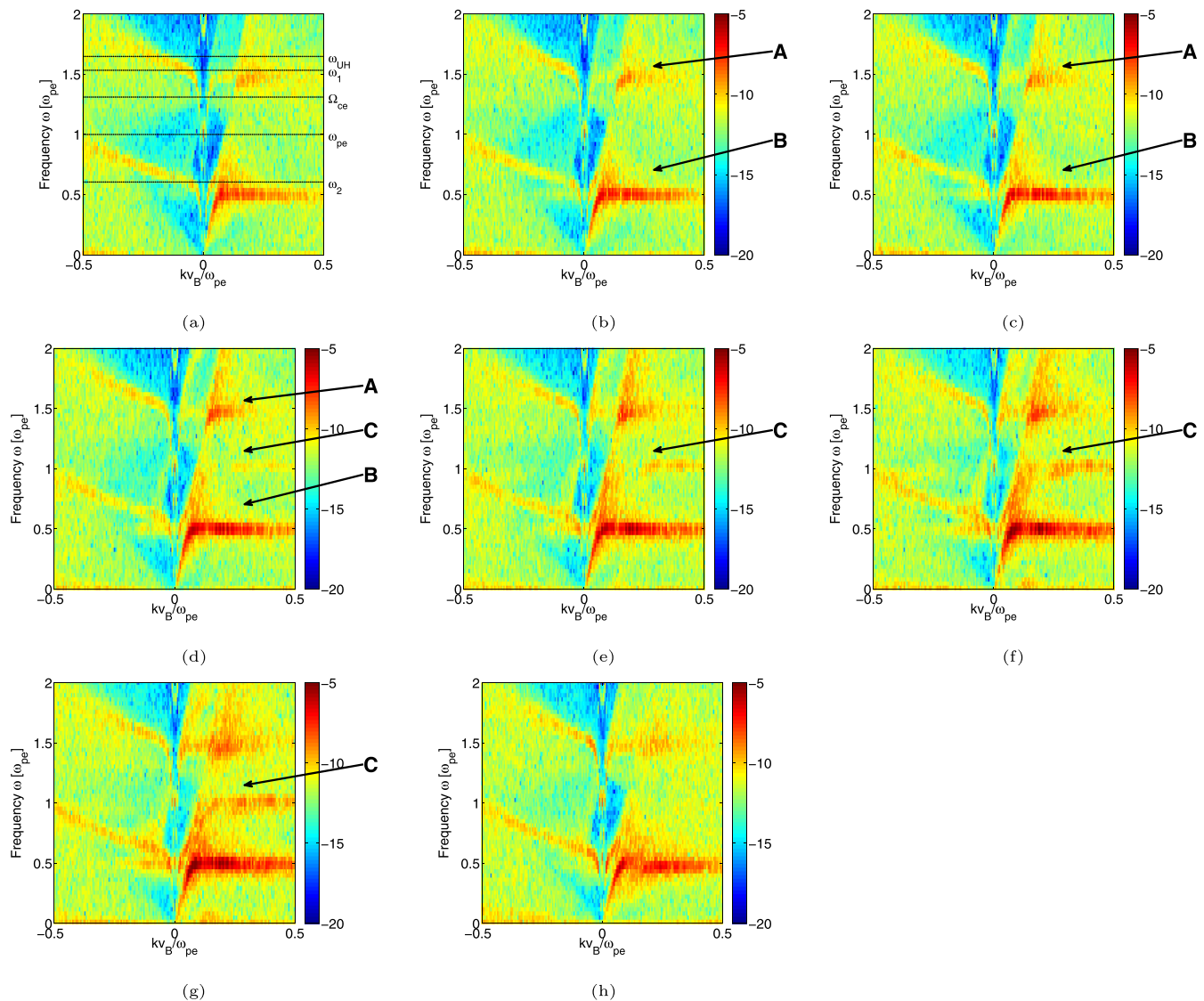


FIG. 3. Time evolution of electrostatic field amplitude, plotted as a function of  $\omega$ ,  $k$  using a logarithmic scale, which is consistent with the electron distribution of Fig. 2. The frequency axis is normalised in units of  $\omega_{pe}$  and the wavenumber axis is represented in units of  $kv_B/\omega_{pe}$ . Panel (a) is constructed by short-time Fourier transforming over the time interval between panels (a) and (b) in Fig. 2, and so on successively for panels (b) to (g), while (h) corresponds to the time interval from  $337.9 \tau_{ce}$  to  $375.4 \tau_{ce}$ . The duration of the Fourier transform time window is the same for all panels in this figure. Panels (a) to (g) correspond to the linear phase of the ADI, see Fig. 6, whereas (h) corresponds to the nonlinear regime. In the upper left panel, the horizontal lines show natural frequencies of the plasma: from top, upper hybrid frequency, higher frequency electrostatic normal mode, electron cyclotron frequency, electron plasma frequency, lower frequency electrostatic normal mode. A, B, and C mark the dominant forward propagating modes in panels (b)-(g). The same colour scale has been adopted in each plot to assist comparison.

This feature may represent a generalisation, previously unobserved in simulations to our knowledge, of a wave-wave resonant form of the anomalous Doppler instability: we note that this class of instability has been suggested<sup>26</sup> as an explanation for the observations<sup>22–25</sup> of fluctuating narrowband emission at  $\omega_{pe}$  from tokamaks. Analytical theory in this area rests on a simple cold beam plasma model,<sup>3,8,26</sup> in which the beam travels relative to the bulk plasma at velocity  $v_0$  parallel to the magnetic field. This differs from the more realistic but less analytically tractable case, considered in the present simulations, of an extended monotonically decreasing suprathermal tail and a thermal bulk population. At present we can only offer a general plausibility argument for the wave-wave resonant hypothesis, in terms of the simple dispersion relation defined by Eq. (5) of

Ref. 8. Resonance between the bulk-supported wave at  $\omega \approx \omega_2$ , in the notation of our Eq. (7), and a negative energy wave supported by the beam at  $\omega \approx k_{\parallel}v_0 - \Omega_{ce}$ , requires<sup>3,8</sup>

$$\omega_2 = k_{\parallel}v_0 - \Omega_{ce}. \quad (9)$$

It is not known how this simple model carries over to the case of an extended monotonically decreasing suprathermal tail combined with a thermal bulk population. In particular, the spectrum of additional natural wave modes arising from the presence of the suprathermal electrons is unknown. Figure 3 gives characteristic parameter values for the spectral feature at  $\omega_{pe}$  of  $kv_B/\omega_{pe} \approx 0.3$  with  $k_{\parallel}/k = 1/\sqrt{2}$  and  $\Omega_{ce}/\omega_{pe} = 1.31$ . Using these values in the resonance condition (9) to infer an effective characteristic velocity  $v_{0,eff}$  for

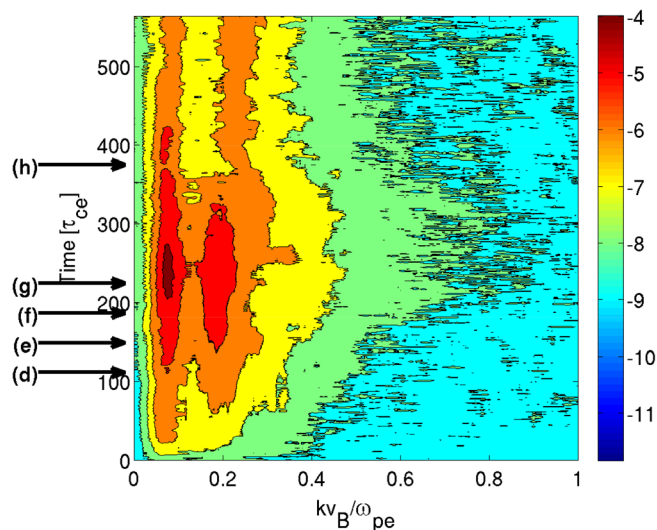


FIG. 4. Growth of dominant modes in  $k$ -space. Contour plot showing the temporal evolution of the dominant electrostatic component of electric field amplitude in  $(k, t)$  space, identified from Fig. 3, in logarithmic scale. (d)–(h) label the corresponding times of panels (d)–(h) in Fig. 2. The signal  $|\mathbf{E}(k, t)|$  is smoothed by averaging over four nearest neighbours.

the tail population yields  $v_{0,eff} \simeq 9.0v_B$ . This value is close to the mean parallel electron velocity of the tail population in the distributions plotted in Fig. 2, from which we infer that wave-wave anomalous Doppler instability may be possible in our simulations.

The temporal evolution of  $|\mathbf{E}(k)|$  for different modes is shown in Figs. 4 and 5. Figure 4 shows that, by  $t \sim 200\tau_{ce}$ , there are two strong enhancements of field energy in  $(k, t)$  space, at  $kv_B/\omega_{pe} = 0.07 \pm 0.02$  and  $kv_B/\omega_{pe} = 0.18 \pm 0.04$ , marked in Fig. 5 as A and B, respectively. The first corresponds to the streaming instability with a parallel phase

velocity equivalent to the mean velocity of the electron tail. Using the spatial domain orientation, here  $\tan\theta = 1$ , and the respective wavenumber  $k$  and wave angular frequency  $\omega_k = \omega_2$  in Eq. (3), we find that the second enhancement corresponds to a parallel phase velocity  $v_{AD}$  whose magnitude is comparable to the maximum tail velocity  $v_M = 17v_B$ . The first two panels in Fig. 5 show the linear phase of ADI, whereas the later two show the development of the nonlinear phase.

The early time evolution of the field amplitude, computed from simulations using different percentage  $\xi$  of energetic electrons, yields linear growth rates whose dependence on  $k$  is shown in Fig. 6. To infer linear growth rates from these PIC simulations, we first identify the linear phase and then evaluate the growth rates via least squares fitting. The resulting empirical scaling of linear growth rate with  $\xi$  is compared in the figure to the analytical scaling (shown in dashed lines) derived by applying Eqs. (A3)–(A7) to each initial  $f$ . As shown in Fig. 6, the simulation linear growth rates agree with the analytical expressions, and follow a decreasing trend with  $k$  as Landau damping becomes more significant as  $k$  increases. Figure 7 shows the temporal development of a particular  $k$  mode for different energetic electron concentrations  $\xi$  in the range 0.02 to 0.1 with other parameters unchanged. The electric field amplitude grows and relaxes at a faster rate for higher  $\xi$ . We have also calculated linear growth rates from PIC simulations with different alignments of the spatial domain with respect to the magnetic field and hence different  $k_{\parallel}/k_{\perp}$ ,  $\tan\theta = 0.5, 1, 3$ , as shown in Fig. 8. Varying the ratio of  $\Omega_{ce}$  to  $\omega_{pe}$  has a similar effect to changing the  $(k_{\perp}, k_{\parallel})$  alignment, as the  $\cos\theta$  term implicit in Eq. (3) effectively modifies the magnitude of  $\Omega_{ce}$  in the resonance condition which defines  $v_{AD}$ . While the condition  $\Omega_{ce} \gg \omega_{pe}$  may simplify the problem analytically, the

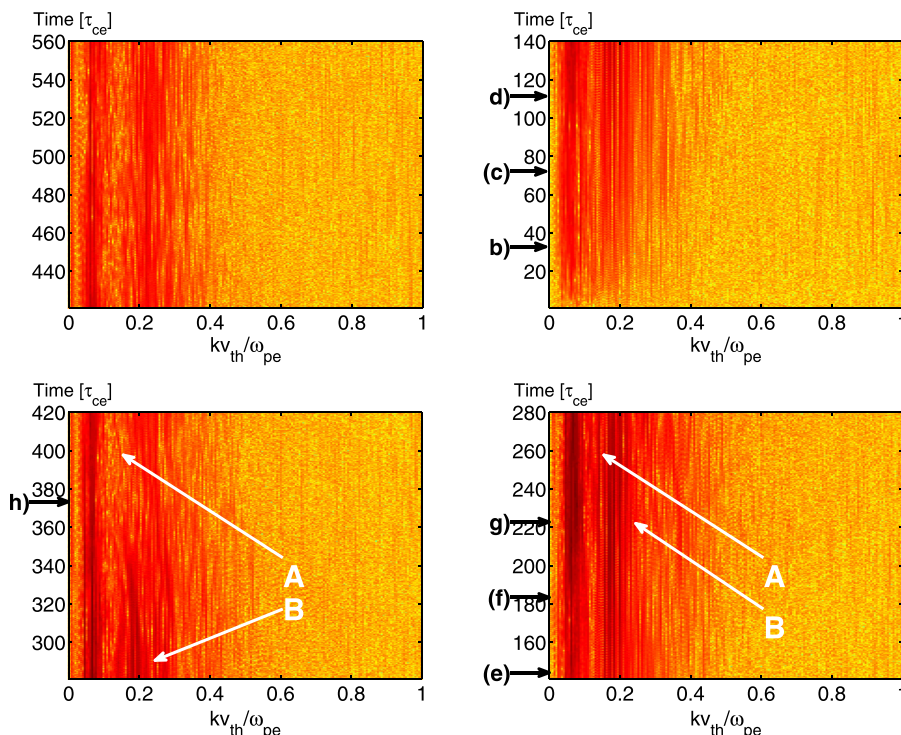


FIG. 5. Four panels showing different time sections of the unsmoothed  $|\mathbf{E}(k, t)|$ , from top right to top left (clockwise) showing time intervals  $t = 0 - 140\tau_{ce}$ ,  $140 - 280\tau_{ce}$ ,  $280 - 420\tau_{ce}$ , and  $420 - 560\tau_{ce}$ . The two dominant modes are marked as A and B. (b)–(h) label the corresponding times of panels (b)–(h) in Fig. 2.

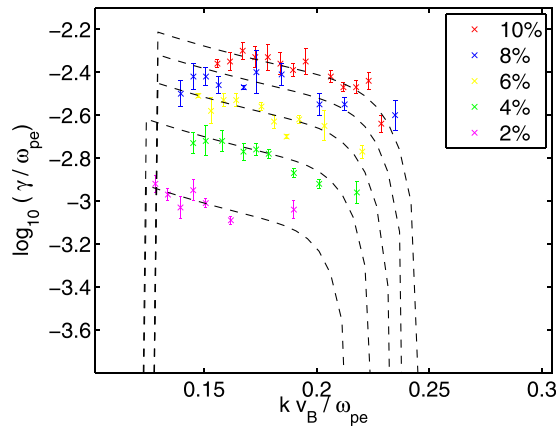


FIG. 6. Comparison between analytical expressions and the growth rates inferred from PIC simulations in their linear regime for flat tails with concentrations  $\xi$  of 2% (pink), 4% (green), 6% (yellow), 8% (blue), and 10% (red). The dashed lines represent the corresponding linear analytical growth rates computed using Eqs. (A3)–(A7). Parameters other than  $\xi$  are the same for all simulations: an initially flat tail with  $v_M = 5.0 \times 10^7 \text{ ms}^{-1}$ ,  $\Omega_{ce}/\omega_{pe} = 1.31$ .

present numerical simulations reveal the existence of instability in cases where  $\Omega_{ce} < \omega_{pe}$ . Thus  $\Omega_{ce} > \omega_{pe}$  is not a necessary condition for the ADI to occur, and the evolution of the electron distribution broadly resembles that of the ADI in Fig. 2.

To quantify the energy transfer between the parallel and perpendicular direction, we evaluate  $\int \mathbf{j}_{\parallel} \cdot \mathbf{E}_{\parallel} dt$  and  $\int \mathbf{j}_{\perp} \cdot \mathbf{E}_{\perp} dt$  by following the trajectories of the bulk and tail electrons from  $t = 0$  up to different times  $\tau$  as shown in Figs. 9 and 10(a), respectively. We define the following quantities for convenience:

$$\epsilon_{\parallel}(\tau) = \int_0^{\tau} j_{\parallel} E_{\parallel} dt, \quad (10)$$

$$\epsilon_{\perp}(\tau) = \int_0^{\tau} j_{\perp} E_{\perp} dt, \quad (11)$$

$$\Delta\epsilon_{\parallel}(\tau, \Delta\tau) = \int_{\tau}^{\tau+\Delta\tau} j_{\parallel} E_{\parallel} dt, \quad (12)$$

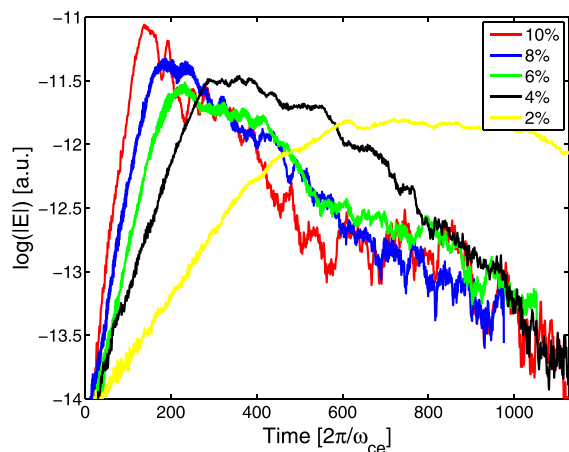


FIG. 7. Temporal evolution of electric field amplitude  $|\mathbf{E}_k(t)|$  of a specific wave-number mode  $kv_B/\omega_{pe} = 0.20$ , for different flat tail concentrations  $\xi$  spanning 2% to 10%. The traces of  $|\mathbf{E}_k(t)|$  are shifted in time such that  $|\mathbf{E}_k(t)|$  for different tail concentrations starts at the same time zero.

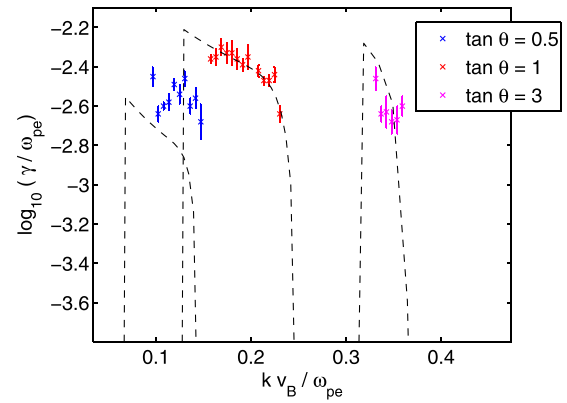


FIG. 8. Dependence of linear-stage growth rate on mode propagation angle with respect to the magnetic field. Coloured points denote linear growth rates of the most strongly growing  $k$ -modes inferred from PIC simulations for  $\Omega_{ce}/\omega_{pe} = 1.31$ . A flat tail with  $\xi = 0.1$  and  $v_M \approx 17v_B$  is used. Dashed lines show analytical linear growth rates for this model, calculated from Eqs. (A3)–(A7).

$$\Delta\epsilon_{\perp}(\tau, \Delta\tau) = \int_{\tau}^{\tau+\Delta\tau} j_{\perp} E_{\perp} dt, \quad (13)$$

where  $\Delta\tau$  is the time interval between data dumps. The current density  $\mathbf{j}$  here refers to the first order moment of the electron distribution function. In particular, the parallel and perpendicular components of the current density of the tail electron population are given by  $j_{\parallel, \text{tail}} = \int_0^{\infty} v_{\parallel} F(v_{\parallel}) dv_{\parallel}$  and  $j_{\perp, \text{tail}} = \int_0^{\infty} v_{\perp} F(v_{\perp}) dv_{\perp}$  which are evaluated using finite sampling in the velocity phase space of the PIC simulations. For the tail electrons,  $\epsilon_{\parallel}(\tau)$  is negative in the rest frame of the simulation throughout the simulation, with the most rapid change during the linear phase of the ADI as shown in Fig. 10(b), while  $\epsilon_{\perp}(\tau)$  increases. Meanwhile both  $\epsilon_{\parallel}(\tau)$  and  $\epsilon_{\perp}(\tau)$  are positive for the bulk electrons and increase throughout the simulation, as shown in Fig. 9. The ratio of  $\epsilon_{\perp}(\tau)$  to  $\epsilon_{\parallel}(\tau)$  for tail electrons is also calculated and shown in the bottom panels of Figs. 10(a) and 10(b) for both the

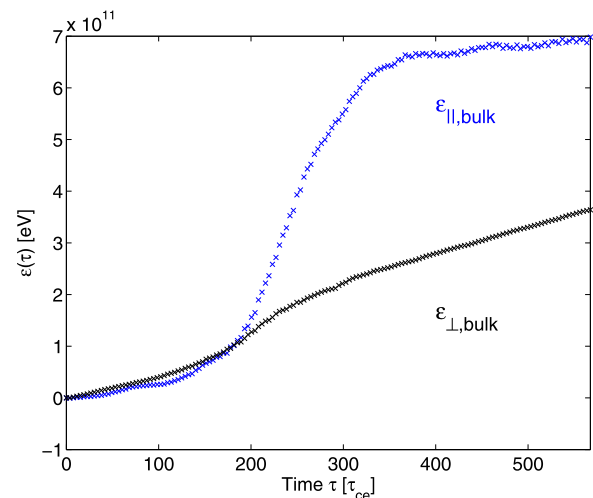


FIG. 9. History of  $\epsilon_{\parallel}$  (blue) and  $\epsilon_{\perp}$  (black) for bulk electron population, computed by following the trajectories of all the bulk electrons throughout the simulation for a flat tail distribution with  $\xi = 0.06$ ,  $\Omega_{ce}/\omega_{pe} = 1.31$  and  $v_M \approx 17v_B$ . Both components of  $\mathbf{j} \cdot \mathbf{E}$  are positive throughout the simulation.

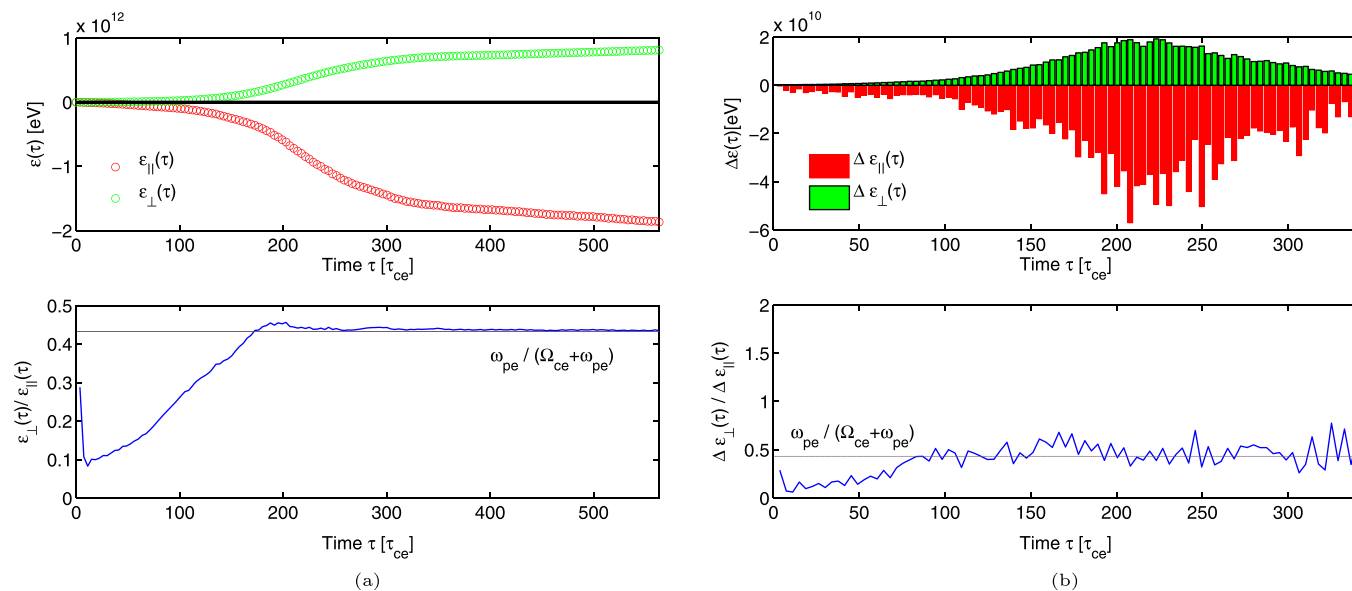


FIG. 10. Energy flow in the perpendicular and parallel directions, over time. (a) Top panel shows the history of  $\epsilon_{\parallel}(\tau)$  (red) and  $\epsilon_{\perp}(\tau)$  (green) computed by following the trajectories of all the tail electrons throughout the simulation. Bottom panel plots the ratio  $|\epsilon_{\perp}(\tau)/\epsilon_{\parallel}(\tau)|$ , the horizontal line marks the value  $\omega_{pe}/(\Omega_{ce} + \omega_{pe})$ . (b) Top panel shows  $\Delta\epsilon_{\parallel}(\tau, \Delta\tau)$  (red) and  $\Delta\epsilon_{\perp}(\tau, \Delta\tau)$  (green) at different times, where  $\Delta\tau$  is the time interval between data dumps which in this case is  $3.78\tau_{ce}$ . Bottom panel shows the ratio  $|\Delta\epsilon_{\perp}/\Delta\epsilon_{\parallel}|$  at each data dump, the horizontal line marks the value  $\omega_{pe}/(\Omega_{ce} + \omega_{pe})$ . An initially flat tail distribution with  $\xi = 0.06$ ,  $\Omega_{ce}/\omega_{pe} = 1.31$  and  $v_M \approx 17v_B$  is used.

aggregate sums and snapshot values. The ratio approaches a steady value of  $\omega_{pe}/(\omega_{pe} + \Omega_{ce})$  during the linear phase of the ADI, hence, a constant proportion of parallel energy is transferred to the perpendicular direction during the linear phase. Previous analytical work<sup>10,12</sup> suggests that this ratio between the energy transfer is  $\Omega_{ce}/(\omega_{pe} + \Omega_{ce})$  in the linear regime of the ADI if the damping terms are neglected. In the present simulations, additional factors, notably damping and nonlinear evolution are fully included. As we have shown, these can become important as electrons evolve away from the magnetic field direction, and this results in values for  $|\epsilon_{\perp}(\tau)/\epsilon_{\parallel}(\tau)|$  that differ significantly from the linear value.

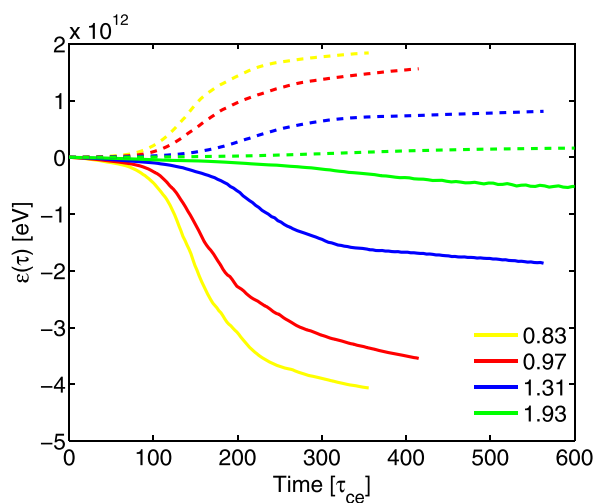


FIG. 11. Time evolution of perpendicular and parallel components of  $\mathbf{j} \cdot \mathbf{E}$  of the tail electrons, for different values of  $\Omega_{ce}/\omega_{pe}$ . The history of  $\epsilon_{\parallel}(\tau)$  (solid lines) and  $\epsilon_{\perp}(\tau)$  (dotted lines) is computed by following the trajectories of all the tail electrons throughout the simulation for a flat tail distribution with  $\xi = 0.08$ , for four different  $\Omega_{ce}/\omega_{pe}$  ratios: 0.83 (yellow), 0.97 (red), 1.31 (blue), and 1.93 (green).

Figure 11 addresses the dependence of ADI phenomenology on the value of the ratio  $\Omega_{ce}/\omega_{pe}$ . It shows the time evolution of  $\epsilon_{\parallel}(\tau)$  and  $\epsilon_{\perp}(\tau)$  in four cases. The magnitude of energy transfer is found to be smaller for larger  $\Omega_{ce}/\omega_{pe}$ , because fewer electrons satisfy the resonance condition, Eq. (3).

Owing to the potential difficulties in creating a flat-tail distribution in some laboratory plasma experimental contexts, the ADI of a monotonically decreasing tail is also of practical interest, and is investigated here. We construct a monotonically decreasing tail distribution by combining populations that have relative parallel drift, as in Eq. (8). Figure 12 shows an example of the time evolution of the electron distribution in such a case. In contrast to the initially flat tail distribution, fan-like spreading out in the high velocity region of  $(v_{\perp}, v_{\parallel})$  phase space is no longer observed. The electron number density at high velocity parallel to  $\mathbf{B}$  declines exponentially in such configurations, leading to a much slower growth rate.

## V. CONCLUSIONS

The anomalous Doppler instability has enduring experimental relevance to magnetically confined fusion plasmas,<sup>5,8,11,14</sup> and to laboratory beam-plasma studies.<sup>17,18,27</sup> Hitherto theoretical interpretation has rested on linear instability analysis and quasilinear approaches. Recent advances in computing resources have now placed the ADI within the scope of contemporary first principles fully self-consistent kinetic simulation. We have performed, for the first time, fully kinetic self-consistent PIC simulations of the ADI for both flat and monotonically decreasing electron tails which capture both linear and nonlinear phases of the ADI. We have performed a systematic comparison between new PIC results and prior analytical theory, and we have established quantitative agreements between the two, spanning the

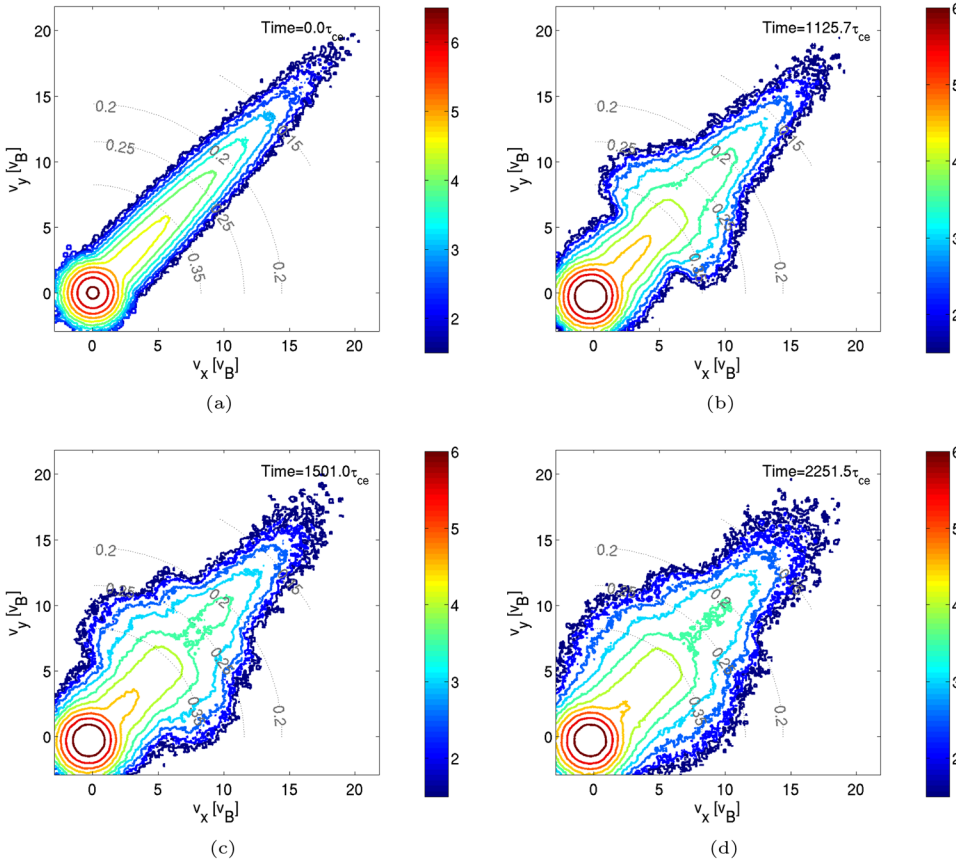


FIG. 12. Snapshots of constant- $f$  contours of an initially monotonically decreasing electron tail distribution, modelled by a shifted Maxwellian with  $\xi = 0.08$ ,  $v_T \approx 9v_B$ ,  $v_D = 0.66v_B$ , and  $\Omega_{ce}/\omega_{pe} = 1.31$  at different times, (a)  $0 \tau_{ce}$ , (b)  $1125.7 \tau_{ce}$ , (c)  $1501.0 \tau_{ce}$ , and (d)  $2251.5 \tau_{ce}$ , for a 8% monotonically decreasing tail. Dashed lines represent constant wavenumber  $v$  contours with normalised wavenumber  $kv_B/\omega_{pe}$  inferred from Eq. (3).

kinetic evolution of the electron distribution and the properties of the self-consistently excited wave fields. We have captured physics beyond the linear phase of the ADI. Specifically, we have: observed the evolution of the thermal bulk population of electrons in response to waves excited by the ADI, which is beyond the reach of analytical theory; followed the ADI through the linear phase to steady state; and obtained the directional components of the  $\mathbf{j} \cdot \mathbf{E}$  energy flow for both bulk and tail electron populations, with damping and nonlinear effects included. The perpendicular and parallel components of the  $\mathbf{j} \cdot \mathbf{E}$  energy flow of tail electrons have been computed for different  $\Omega_{ce}/\omega_{pe}$  ratios and, interestingly, we find that the ADI can arise beyond the previously expected parameter range, in particular where  $\Omega_{ce} < \omega_{pe}$ . The simulations also exhibit a spectral feature which may correspond to the observations of suprathermal narrowband emission at  $\omega_{pe}$  detected from low density tokamak plasmas. Our model results suggest that this may be compatible with an explanation in terms of wave-wave resonant anomalous Doppler instability.

It is clear from the present work that the ADI joins other key collective effects involving energetic electrons in tokamak plasmas, such as alpha channelling,<sup>16</sup> in benefitting from PIC simulations. There is a firm basis for integrating the ADI approach presented here into more comprehensive models of energetic electron phenomenology in magnetically confined fusion and laboratory plasmas. Predicting the role of energetic electron populations in ITER has been a focus of experimental and theoretical work since the mid-1990s,<sup>28,29</sup> and remains topical.<sup>30</sup>

## ACKNOWLEDGMENTS

This work was part-funded by the RCUK Energy Programme under Grant EP/I501045 and the European Communities under the contract of Association between EURATOM and CCFE. The views and opinions expressed herein do not necessarily reflect those of the European Commission. The EPOCH code used in this work was developed as part of an EPSRC funded project, Grant No. EP/G054950/1.

## APPENDIX: ANALYTICAL LINEAR THEORY

The analytical linear growth rate of electrostatic waves generated by the ADI is obtained<sup>10</sup> from the full electrostatic dielectric response function given by<sup>31</sup>

$$\begin{aligned} \epsilon = 1 - \frac{\omega_{pe}}{k^2} \sum_{n=-\infty}^{\infty} \int_{v_{\parallel}=-\infty}^{\infty} \int_{v_{\perp}=0}^{\infty} \frac{2\pi v_{\perp} dv_{\perp} dv_{\parallel}}{n\Omega_{ce} + k_{\parallel}v_{\parallel} - \omega} \\ \times \left( \frac{n\Omega_{ce}}{v_{\perp}} \frac{\partial f}{\partial v_{\perp}} + k_{\parallel} \frac{\partial f}{\partial v_{\parallel}} \right) J_n^2 \left( \frac{k_{\perp} v_{\perp}}{\Omega_{ce}} \right) \\ - \frac{\omega_{pi}^2}{k} \int_{v_i=-\infty}^{\infty} \frac{dv_i}{kv_i - \omega} \frac{df_i}{dv_i}. \end{aligned} \quad (\text{A1})$$

Here,  $(v_{\parallel}, v_{\perp})$  denote the velocities parallel and perpendicular to the magnetic field  $\mathbf{B}$ ;  $f(v_{\parallel}, v_{\perp})$  is the electron distribution function and  $f_i(v_i)$  that of the ions;  $\Omega_{ce}$  and  $\omega_{pe}$  are the electron cyclotron and plasma frequency, respectively; and  $(k_{\parallel}, k_{\perp})$  denote the wavenumber components parallel and

perpendicular to the magnetic field. A spatially uniform equilibrium plasma is assumed. Following,<sup>10</sup> we decompose the electron velocity distribution into a majority thermal Maxwellian bulk and a much smaller (fraction  $\xi \ll 1$ ) supra-thermal tail distribution  $F(v_{\parallel})$ :

$$f(v_{\perp}, v_{\parallel}) = \frac{1 - \xi}{\pi^{3/2} v_B^3} e^{-v_{\perp}^2/v_B^2} e^{-v_{\parallel}^2/v_B^2} + \frac{\xi}{\pi v_{T\perp}^2} e^{-v_{\perp}^2/v_{T\perp}^2} F(v_{\parallel}), \quad (\text{A2})$$

where  $v_B$  represents the thermal velocity of the Maxwellian bulk electrons and  $v_{T\perp}$  is the perpendicular thermal velocity which is the same as  $v_B$  in our simulation setup. To simplify, we consider  $\Omega_{ce} \gg \omega_{pe}$ , in which case the lower electrostatic mode  $\omega_2$  dominates and can be approximated as  $\omega_{pe} k_{\parallel}/k$ . The growth rate of the mode at  $\omega_1$  is less than that at  $\omega_2$  by a factor  $\Omega_{ce}/\omega_{pe}$ ,<sup>32</sup> hence, we shall focus on the growth rate of the lower mode with real frequency  $\omega_2 = \omega_{pe} k_{\parallel}/k$ . Substituting the above expression into the electrostatic dielectric response function yields the contributions to linear growth and damping given by Eqs. (A3) to (A7) of Ref. 10, reproduced here for convenience:

$$\frac{\gamma}{\omega_{pe}} = \frac{\gamma_{AD}}{\omega_{pe}} - \left( \frac{\gamma_{LB}}{\omega_{pe}} + \frac{\gamma_{LT}}{\omega_{pe}} + \frac{\gamma_{LI}}{\omega_{pe}} \right), \quad (\text{A3})$$

$$\begin{aligned} \frac{\gamma_{AD}}{\omega_{pe}} &= \xi \pi^{1/2} \left( \frac{\omega_{pe}}{k v_B} \right)^2 \Gamma_1(\beta_T) \\ &\times \left[ \frac{\Omega_{ce}}{k v_B} \left( \frac{v_B}{v_{T\perp}} \right)^2 \pi^{1/2} v_B F(v_{\parallel}) + \frac{k_{\parallel} \pi^{1/2} v_B^2}{k} \frac{dF}{dv_{\parallel}} \right]_{v_{\parallel}=v_{AD}}, \end{aligned} \quad (\text{A4})$$

$$\frac{\gamma_{LB}}{\omega_{pe}} = (1 - \xi) \pi^{1/2} \left( \frac{\omega_{pe}}{k v_B} \right)^3 \Gamma_0(\beta_B) \frac{k_{\parallel}}{k} e^{-\left(\frac{\omega_{pe}}{k v_B}\right)^2}, \quad (\text{A5})$$

$$\frac{\gamma_{LT}}{\omega_{pe}} = \xi \pi^{1/2} \left( \frac{\omega_{pe}}{k v_B} \right)^2 \Gamma_0(\beta_T) \frac{k_{\parallel}}{k} \left( -\frac{\pi^{1/2} v_B^2}{2} \frac{dF}{dv_{\parallel}} \right)_{v_{\parallel}=\omega_{pe}/k}, \quad (\text{A6})$$

$$\frac{\gamma_{LI}}{\omega_{pe}} = \pi^{1/2} \left( \frac{\omega_{pe}}{k v_B} \right)^3 Z \left( \frac{m_i}{m_e} \right)^{1/2} \left( \frac{k_{\parallel}}{k} \right)^2 e^{-\left(\frac{\omega_{pe}}{k v_B}\right)^2 \frac{m_i}{m_e} \left( \frac{k_{\parallel}}{k} \right)^2}. \quad (\text{A7})$$

Here  $\Gamma_n(x) = e^{-x} I_n(x)$ , where  $I_n$  denotes the modified Bessel function of order  $n$ ,  $Z$  is the ion charge state,  $\beta_B = k_{\perp}^2 v_B^2 / 2 \Omega_{ce}^2$ , and  $\beta_T = (v_{T\perp}^2 / v_B^2) \beta_B$ . Equation (A7) describes Landau damping on a thermal ion population with characteristic temperature equal to that of the bulk electrons.

- <sup>1</sup>V. L. Ginzburg, *Sov. Phys. Usp.* **2**, 874 (1960).
- <sup>2</sup>V. L. Ginzburg, *Sov. Phys. JETP* **35**, 92 (1972).
- <sup>3</sup>M. V. Nezlin, *Sov. Phys. Usp.* **19**, 946 (1976).
- <sup>4</sup>V. V. Parail and O. P. Pogutse, *Sov. J. Plasma Phys.* **2**, 126 (1976).
- <sup>5</sup>K. Molvig, M. S. Tekula, and A. Bers, *Phys. Rev. Lett.* **38**, 1404 (1977).
- <sup>6</sup>V. V. Parail and O. P. Pogutse, *Nucl. Fusion* **18**, 303 (1978).
- <sup>7</sup>H. Knoepfel and D. A. Spong, *Nucl. Fusion* **19**, 785 (1979).
- <sup>8</sup>S. C. Liu, V. S. Chan, D. K. Bhadra, and R. W. Harvey, *Phys. Rev. Lett.* **48**, 1479 (1982).
- <sup>9</sup>R. O. Dendy and C. N. Lashmore-Davies, *Plasma Phys. Controlled Fusion* **26**, 1347 (1984).
- <sup>10</sup>R. O. Dendy, C. N. Lashmore-Davies, and A. Montes, *Phys. Fluids* **29**, 4040 (1986).
- <sup>11</sup>S. C. Luckhardt, K.-I. Chen, M. J. Mayberry, M. Porkolab, Y. Terumichi, G. Bekefi, F. S. McDermott, and R. Rohatgi, *Phys. Fluids* **29**, 1985 (1986).
- <sup>12</sup>R. O. Dendy, *Phys. Fluids* **30**, 2438 (1987).
- <sup>13</sup>T. Fulop, G. Pokol, P. Helander, and M. Lisak, *Phys. Plasmas* **13**, 062506 (2006).
- <sup>14</sup>S. Sajjad, X. Gao, B. Ling, S. H. Bhatti, and T. Ang, *Phys. Plasmas* **17**, 042504 (2010).
- <sup>15</sup>Y. M. Wang, X. Gao, L. Ling, Y. Liu, S. B. Zhang, X. Han, A. Ti, E. Z. Li, and HT-7 Team, *Phys. Plasmas* **19**, 032509 (2012).
- <sup>16</sup>J. W. S. Cook, S. C. Chapman, and R. O. Dendy, *Phys. Rev. Lett.* **105**, 255003 (2010).
- <sup>17</sup>K. Ronald, S. L. McConville, D. C. Speirs, A. D. R. Phelps, C. W. Robertson, C. G. Whyte, W. He, K. M. Gillespie, A. W. Cross, and R. Bingham, *Phys. Plasmas* **15**, 056503 (2008).
- <sup>18</sup>K. Ronald, S. L. McConville, D. C. Speirs, A. D. R. Phelps, C. W. Robertson, C. G. Whyte, W. He, K. M. Gillespie, A. W. Cross, and R. Bingham, *Plasma Sources Sci. Technol.* **17**, 035011 (2008).
- <sup>19</sup>R. Bingham, R. A. Cairns, I. Vorgul, and V. D. Shapiro, *J. Plasma Phys.* **76**, 539 (2010).
- <sup>20</sup>R. O. Dendy, *Plasma Phys. Controlled Fusion* **33**, 1069 (1991).
- <sup>21</sup>A. B. Mikhailovskii, *Theory of Plasma Instabilities, Vol 1: Instabilities of a Homogeneous Plasma* (Springer, 1974).
- <sup>22</sup>A. E. Costley and T. Group, *Phys. Rev. Lett.* **38**, 1477 (1977).
- <sup>23</sup>I. H. Hutchinson and S. E. Kissel, *Phys. Fluids* **23**, 1698 (1980).
- <sup>24</sup>R. F. Gandy and D. H. Yates, *Phys. Fluids* **28**, 1877 (1985).
- <sup>25</sup>R. F. Gandy, I. H. Hutchinson, and D. H. Yates, *Phys. Rev. Lett.* **54**, 800 (1985).
- <sup>26</sup>R. O. Dendy, C. N. Lashmore-Davies, and M. M. Shoucri, *Nucl. Fusion* **25**, 721 (1985).
- <sup>27</sup>R. Bryson, I. Vorgul, R. A. Carins, D. C. Speirs, M. King, K. Ronald, A. D. R. Phelps, R. Bingham, S. L. McConville, K. M. Gillespie, and A. W. Cross, See <http://ocs.ciemat.es/epsicpp2012pap/pdf/P1.158.pdf> for "Proceedings of the 2012 EPS Conference on Plasma Physics, P1.158."
- <sup>28</sup>R. Jaspers, N. J. Lopes Cardozo, F. C. Schuller, K. H. Finken, T. Grewe, and G. Mank, *Nucl. Fusion* **36**, 367 (1996).
- <sup>29</sup>S. Putvinski, P. Barabaschi, N. Fujisawa, N. Putvinskaya, M. N. Rosenbluth, and J. Wesley, *Plasma Phys. Controlled Fusion* **39**, B157 (1997).
- <sup>30</sup>K. O. Aleynikova, P. B. Aleynikov, S. V. Kononov, A. A. Teplukhina, and V. E. Zhogolev, See <http://ocs.ciemat.es/EPS2013PAP/pdf/O5.103.pdf> for "Proceedings of the 2013 EPS Conference on Plasma Physics, O5.103."
- <sup>31</sup>N. A. Krall and A. W. Trivelpiece, *Principles of Plasma Physics* (San Francisco Press, 1986).
- <sup>32</sup>A. I. Akhiezer, I. A. Akhiezer, R. V. Polovin, A. G. Sitenko, and K. N. Stepanov, *Plasma Electrodynamics, Vol. 2: Non-Linear Theory and Fluctuations* (Pergamon Press, Oxford, 1975).